

pubs.acs.org/JACS Article

# Charge Transfer and Chemo-Mechanical Coupling in Respiratory Complex I

Chitrak Gupta, Umesh Khaniya, Chun Kit Chan, Francois Dehez, Mrinal Shekhar, M. R. Gunner, Leonid Sazanov,\* Christophe Chipot,\* and Abhishek Singharoy\*



Cite This: J. Am. Chem. Soc. 2020, 142, 9220-9230



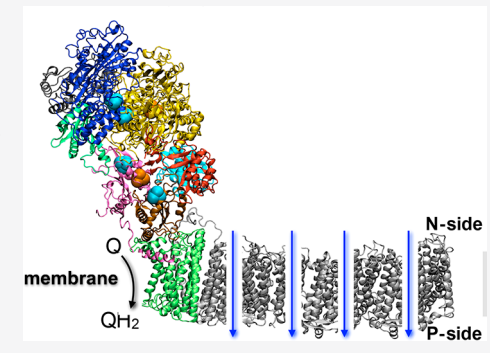
**ACCESS** 

Metrics & More

Article Recommendations

Supporting Information

ABSTRACT: The mitochondrial respiratory chain, formed by five protein complexes, utilizes energy from catabolic processes to synthesize ATP. Complex I, the first and the largest protein complex of the chain, harvests electrons from NADH to reduce quinone, while pumping protons across the mitochondrial membrane. Detailed knowledge of the working principle of such coupled charge-transfer processes remains, however, fragmentary due to bottlenecks in understanding redox-driven conformational transitions and their interplay with the hydrated proton pathways. Complex I from *Thermus thermophilus* encases 16 subunits with nine iron—sulfur clusters, reduced by electrons from NADH. Here, employing the latest crystal structure of *T. thermophilus* complex I, we have used microsecond-scale molecular dynamics simulations to study the chemo-mechanical coupling between redox changes of the iron—sulfur clusters and conformational transitions across complex I. First, we identify the redox switches within complex I, which allosterically



couple the dynamics of the quinone binding pocket to the site of NADH reduction. Second, our free-energy calculations reveal that the affinity of the quinone, specifically menaquinone, for the binding-site is higher than that of its reduced, menaquinol form—a design essential for menaquinol release. Remarkably, the barriers to diffusive menaquinone dynamics are lesser than that of the more ubiquitous ubiquinone, and the naphthoquinone headgroup of the former furnishes stronger binding interactions with the pocket, favoring menaquinone for charge transport in *T. thermophilus*. Our computations are consistent with experimentally validated mutations and hierarchize the key residues into three functional classes, identifying new mutation targets. Third, long-range hydrogen-bond networks connecting the quinone-binding site to the transmembrane subunits are found to be responsible for proton pumping. Put together, the simulations reveal the molecular design principles linking redox reactions to quinone turnover to proton translocation in complex I.

#### INTRODUCTION

Cellular respiration converts chemical energy extracted from nutrients into mechanical energy necessary for the synthesis of ATP, the energy currency of life. The terminal step of respiration involves the so-called oxidative phosphorylation (OXPHOS) reactions. Occurring within the mitochondrial membrane, OXPHOS harnesses the energy produced by catabolic processes, namely glycolysis, fatty acid oxidation, and the tricarboxylic acid (TCA) cycle to regenerate ATP molecules. Bacterial and mitochondrial energy conversions are achieved by a network of five respiratory chain enzymes, denoted complexes I through V.

Complex I (NADH:ubiquinone oxidoreductase) is the first and the largest protein complex of the mitochondrial respiratory chain, illustrated in Figure 1. Atomic structures of this complex reveal an L-shaped organization of 14–16<sup>2,3</sup> and 45<sup>4</sup> subunits, in bacteria and mammals, respectively, distributed between a water-soluble and a transmembrane (TM) arm. The former, or peripheral-arm, extracts two electrons from NADH, an energy-rich product of the TCA

cycle. These two electrons are transferred through eight conserved iron—sulfur clusters (six  $Fe_4S_4$  and two  $Fe_2S_2$ ) to a quinone docked to its binding site. An additional  $Fe_4S_4$  cluster termed N7 is off the main redox pathway. The addition of two electrons and two protons reduces this charge-carrier to quinol. The protons bound to the quinone do not add to the proton gradients, as they come from the same N—side (negative, high pH) of the membrane as the electrons. However, conformational changes arising from the double quinone reduction induce pumping of four protons across the TM arm from the N-side to the P-side (positive, low pH) of the membrane. This proton gradient is utilized for downstream synthesis of ATP by complex V. $^{5,6}$  The chemo-mechanical coupling or chemically

Received: December 13, 2019 Published: April 29, 2020





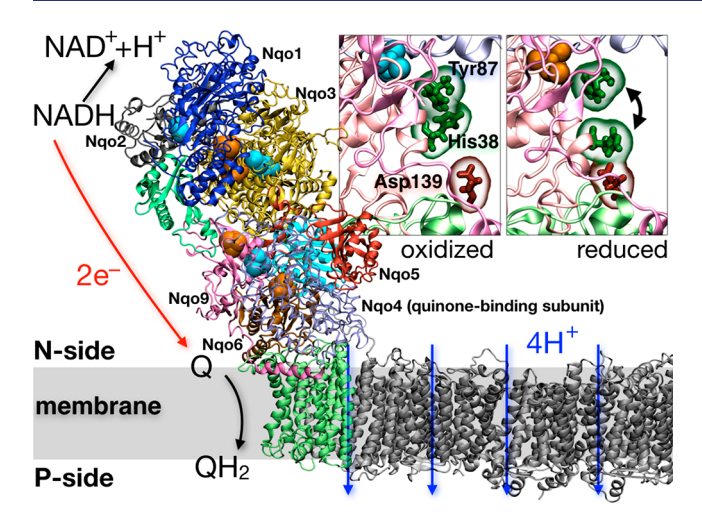


Figure 1. Crystal structure of complex I. Soluble domain of complex I is colored by subunits. NADH-binding subunit is shown in blue. Iron—sulfur clusters are shown in orange (reduced) or cyan (oxidized). Quinone headgroup-binding subunit is shown in ribbon representation for clarity. The TM part is shown in silver, except for quinone tail-coordinating subunit Nqo8 in green. Inset: Quinone-binding cavity along with the nearest iron—sulfur cluster. Highlighted are the binding site residues Nqo4 His38 (green) and Nqo4 Tyr87 (green), along with the nearby Nqo4 Asp139 (red). When the nearest iron—sulfur cluster (N2) is oxidized (left), the binding site is closed. When it is reduced (right), the binding site opens up to facilitate quinone insertion.

induced mechanical events in complex I occur over time scales ranging from those of electron dynamics, which span picoseconds (ps), to those of conformational transitions and membrane-wide diffusion, in excess of milliseconds (ms). These processes are extremely efficient in terms of energy conversion.<sup>7,8</sup> Mutations impacting these conversion steps are implicated in a number of mitochondrial disorders.<sup>9</sup>

Owing to the ubiquity of complex I in aerobic respiratory pathways 10 and its remarkable efficiency as a conduit for biological energy transfer, a large number of investigations have been performed.<sup>2,11–16</sup> Observed locations and orientations of the iron-sulfur clusters in the soluble arm and polar residues in the TM arm have prompted several hypotheses <sup>17,18</sup> on the possible pathways of electron transfer and proton pumping. For example, Verkhovskaya et al. 17 have hypothesized that the first electron donated by NADH is transferred to the iron-sulfur cluster N2 nearest the quinone at electron tunneling rates, and that this transfer is independent from the proton-pumping events, while the arrival of a second electron and the subsequent Q protonation are linked to proton pumping. Some of the conjectured pathways have been probed in mutational experiments, 17,19 but a comprehensive picture is yet to be determined in view of the following inconsistency. Seven of the eight iron-sulfur clusters are within 14 Å of each other, which is a distance germane to direct electron transfer.<sup>2,20</sup> In addition, the time scale of electron transfer across the eight conserved clusters is estimated<sup>7</sup> and measured  $^{17}$  to be ca. 100  $\mu$ s. Yet, each catalytic cycle in complex I spans ca. 5 ms, 21 which suggests that there must be additional factors at play, aside from the redox reaction itself, responsible for complex I turnover. Here, we address how reduction of the Fe<sub>4</sub>S<sub>4</sub> clusters induces large-scale subunit motions in the soluble arm of complex I, and provide a possible explanation for the ms-time scale energy storage. In

doing so, we justify the necessity of an elaborate eight-cluster electron-transfer machinery in complex I.

The binding site for the amphipathic quinone is ca. 20-30 Åabove the membrane plane, 3,22 unlike in most other quinone reductases, where the charge carrier has an easy access to the binding site from the hydrophobic core of the membrane. In addition, the quinone is ca. 40-160 Å away from the sites of proton pumping,<sup>3</sup> which raises questions about the connection between binding of the charge carrier and proton transport. Here, we ask how quinone binding and reduction regulate the dynamics of the soluble arm and the TM subunits via concerted water networks. It is noteworthy that in contrast with recent investigations involving ubiquinone, 12 we have employed the more biologically relevant menaquinone (the native Thermus thermophilus quinone containing 8 isoprenyl units) in the present work. Moreover, the redox state of the iron-sulfur clusters was derived from the compendium of EPR, <sup>17</sup> DEER, <sup>23</sup> and Mossbauer spectroscopy results, <sup>19</sup> ensuring that they are not all-reduced or singly reduced, but rather reflect a stationary state of electron flux, wherein four (N3, N4, N6a, N2, as per the traditional nomenclature<sup>2</sup>) Fe<sub>4</sub>S<sub>4</sub> clusters are reduced and the three remaining clusters from the main redox chain connecting FMN and Q, oxidized. Henceforth, "reduced complex I" denotes the state where N3, N4, N6a, and N2 clusters are reduced. A more detailed rationale for this choice is provided in the Methods section.

In this work, we combine an aggregate 17.8  $\mu$ s of molecular dynamics (MD) simulations and free-energy calculations to decrypt the redox-controlled chemo-mechanical coupling in complex I, and address the long-range communication between the NADH-binding and quinone-reduction sites. In agreement with the experiments, 4,24 the present theoretical investigation captures both the local and global conformational changes induced by the reduction of two different sets of iron—sulfur clusters, and illuminates the impact of these changes on quinone and water dynamics.

## ■ RESULTS AND DISCUSSION

In what follows, we describe the chemo-mechanical coupling in the soluble part of complex I, employing a variety of computational tools suitable to capture the large-scale conformational transitions at protein—protein and protein—water interfaces. These simulations will illuminate the allosteric pathways that (i) begin with local changes in the electric field created by the  $Fe_4S_4$  clusters, (ii) promote the opening and closing of the quinone/quinol binding pocket, and (iii) enable charge displacement from the binding site into the first proton-pumping channel, namely the E-channel.<sup>3</sup>

Redox-Induced Side-Chain Switches Control the Dynamics of the Soluble Arm of Complex I. Two sets of separate 1.5  $\mu$ s MD simulations were carried out on complex I in the apo form, devoid of menaquinone, with Fe<sub>4</sub>S<sub>4</sub> clusters oxidized or reduced. The protein appears to exist in distinct conformations between the oxidized and reduced states. While the structure of the oxidized complex I is closer to that in the crystal (PDB: 4HEA), the Nqo2 and Nqo5 subunits of the reduced structure undergo a significant rotation by 4°–8° (Figure 2A). Thus, the soluble part of a reduced complex I is more open than the oxidized form, with looser protein—protein interfaces (Figure 2B), as also observed experimentally with an isolated soluble arm.<sup>24</sup> Concomitantly, the quinone-binding pocket is more open in a reduced apo structure than in the oxidized form (Figure 1 (inset) and Figure S1 of the

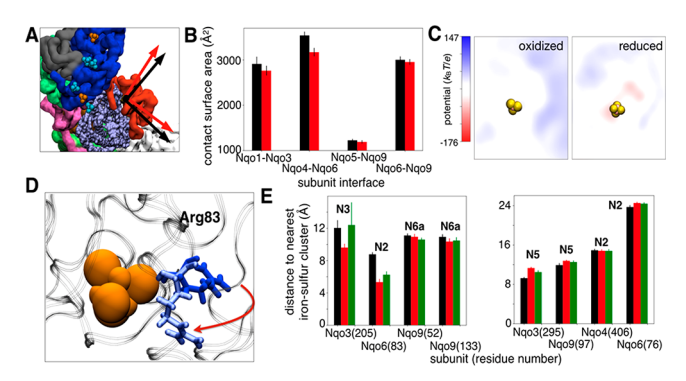


Figure 2. Origin of redox-induced concerted motion in complex I. (A) Change in the direction of the principal component of subunit Ngo5 with respect to the initial structure (black: oxidized, red: reduced). Reduction-induced subunit reorientation results in rotation of the subunits. (B) Intersubunit contact surface area in the oxidized (black) and reduced (red) complex I. Reduction of the Fe<sub>4</sub>S<sub>4</sub> clusters causes the subunits to move away from each other, resulting in a decrease of the contact surface area. Also see Figure S2. (C) Electrostatic map near a typical Fe<sub>4</sub>S<sub>4</sub> cluster N2 (left: oxidized, right: reduced). The electrostatic environment is sensitive to the redox state of the Fe<sub>4</sub>S<sub>4</sub> cluster and the potential changes from +147  $k_BT/e$  to  $-176 k_B T/e$ . (D) Redox-driven motion of one of the redox-switches, Arg83 of subunit Ngo6, is shown. The positively charged Arg side chain moves closer to the nearest Fe<sub>4</sub>S<sub>4</sub> cluster when it is reduced (orange). (E) Distance of the Arg and Lys switches from their nearest Fe<sub>4</sub>S<sub>4</sub> cluster (black: oxidized, red: reduced, green: oxidized reinitialized from reduced). The Fe<sub>4</sub>S<sub>4</sub> clusters are specified on the top of each bar. Reduction causes local motion resulting in the nearby basic residues (Arg205, Arg83, Lys52, and Lys133) to move closer or farther from the Fe<sub>4</sub>S<sub>4</sub> cluster. Impact of redox changes on the acidic residues (Asp406 and Asp76) conformations is opposite and less pronounced (see Figure S3).

Supporting Information, SI). Described below, the coupling between the dynamics of subunit Nqo4 and that of the binding pocket underscores the role of long-range interactions in tuning the quinone traffic within complex I.

Reminiscent of single-electron transfer at the interface of cytochrome  $c_2$  and complex III, <sup>25</sup> the redox states of the Fe<sub>4</sub>S<sub>4</sub> clusters control the conformation of the quinone-binding site through concerted motions of lysine and arginine residues at the protein-protein interface. Due to the change in the electrostatic environment of the reduced Fe<sub>4</sub>S<sub>4</sub> clusters (Figure 2C), the positively charged residues (either Arg or Lys) in their vicinity are attracted toward them (Figure 2D,E). Similarly, the acidic Asp residues are repelled by the reduced Fe<sub>4</sub>S<sub>4</sub> clusters. Particle Mesh Ewald (PME) computations indicate that the basic residues Nqo3 Arg205, Nqo6 Arg83, Nqo9 Lys52, and Nqo9 Lys133 isomerize, approaching three of the four reduced Fe<sub>4</sub>S<sub>4</sub> clusters, while moving away from the other three oxidized ones (see Figures 2E and S3). Henceforth, these redox-sensitive isomerizing residues are referred to as switches. Remarkably, such titratable switch residues also line the interface between the Nqo3, Nqo6, and Nqo9 subunits of the soluble domain of complex I. The network analysis illustrated in Figure 3A reveals that the switches formed by these basic residues also serve as interaction vertices between highly correlated protein subunits. Consequently, isomerization of the lysine and arginine switches loosens the subunit-subunit interfaces of reduced complex I. Strong correlation between the local and global interaction energy changes (Figure 3B,C) further confirms that subunit reorganization originates from

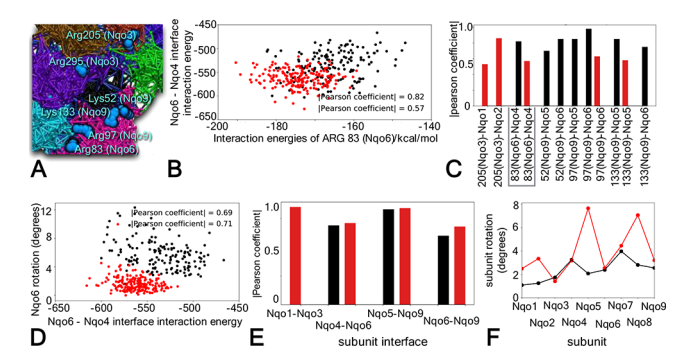


Figure 3. Global changes in interaction energies are correlated to the subunit rotation. (A) Network analysis showing the different regions that move in a correlated fashion. Residues identified in panel B are highlighted in blue. These residues line the boundary between the correlated subunits. (B) Correlation between interaction energy of Arg83 of subunit Nqo6 with its environment and the interaction energy between subunits Nqo6 and Nqo4 (black: oxidized, red: reduced). In both oxidized and reduced complex I, there is a strong correlation (albeit of opposite signs), demonstrating how local redox changes affect global (subunit-subunit) interaction energies. (C) Similar correlation coefficients between interaction energy of residues with its environment and the interaction energy between subunits (black: oxidized, red: reduced). X-axis labels show the specific residue number, followed by the subunit in parentheses, and finally the subunit whose interface is affected. (D) Correlation between interaction energy between subunits Ngo6 and Ngo4 and the rotation of the Nqo6 subunit (black: oxidized, red: reduced). Both oxidized and reduced complex I shows strong correlation, demonstrating how global interaction energies effect subunit reorientation. (E) Similar correlation coefficients of other subunit interfaces and subunit rotations. X-axis labels show the specific subunit-subunit interface (rotation is experienced by the second subunit in each case). (F) Change in the direction of the principal component of the subunits with respect to the initial structure, at the end of the simulation (black: oxidized, red: reduced). Reduction causes significant changes to the orientation of the subunits. Also see Figure S5.

side chain rearrangements. In turn, the associated global energy changes are correlated with the rigid-body-like rotation of the subunits (Figure 3D–F). Consistent with this correlation, subunits forming interfaces with a larger number of basic switches undergo accordingly more significant rotation (Figure 2A). For example, Nqo3 and Nqo9 interface with, respectively, two and three switch residues, and undergo maximum internal deformation (Figures 2E and 4A).

Entry of water through the gap formed by rotated protein subunits stabilizes loose contacts (see Figure S4), thereby conferring to the soluble arm more flexibility in the reduced complex I (see Figure 4A). In particular, subunit Nqo4, which subsumes two reduced Fe<sub>4</sub>S<sub>4</sub> clusters, i.e., N2 and N6a, experiences a hinge-bending-like motion (see Figure 4C) between two dynamically distinct subnetworks (see Figure 3A) embedded within the same protein chain. In the oxidized state, the entire Nqo4 chain only engenders a single concerted network bereft of hinge-bending movement (see Figure 4D), which implies a more rigid conformation than in the reduced state. Noteworthily, the same chain harbors the menaquinone/ menaquinol binding site, made accessible through the hingebending motion brought to light herein. The redox-induced dynamical correlation between the soluble domains, therefore, directly modulates the local conformation of the quinone-

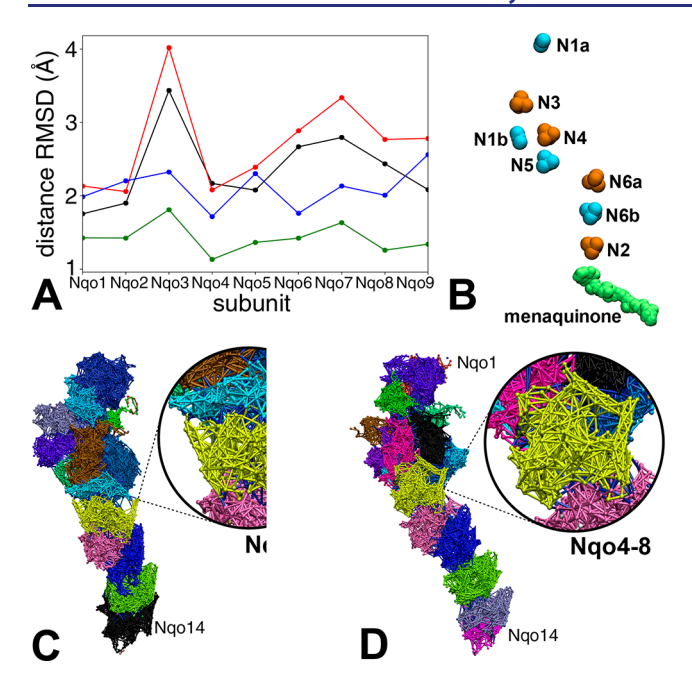


Figure 4. Redox-coupled local motion in Complex I. (A) Internal RMSD of individual subunits with respect to the initial structure, PDB ID 6Y11 (black: oxidized, red: reduced, blue: quinone-bound, oxidized, green: quinone-bound, reduced). Quinone-binding causes the subunits, especially Nqo3, to be more stable (less dynamic) compared to apo Complex I. Note that the protein structure underwent significant changes after quinone-docking. Hence, the initial structure of the apo and quinone-bound molecules was different. (B) Location of the FeS clusters (cyan: oxidized, orange: reduced) and quinone (green). (C, D) Comparison of the network model between reduced (left) and oxidized (right) Complex I. Reduction causes a split in the network near the binding site in Nqo4 (yellow + cyan in reduced, yellow in oxidized). This split in correlated motion causes the opening of the Q binding pocket upon reduction.

binding pocket by mediating the flexibility of the Nqo4 subunit.

To confirm this observation, the final frames from the three replicas of the 500 ns long MD simulation featuring four reduced  $Fe_4S_4$  clusters were extracted, and the simulations were continued for another 800 ns, wherein all the eight clusters are in an oxidized state. During these simulations, the lysine switches move in opposite directions (Figures 2E and S3), closing the quinone pocket (Figure S1). Furthermore, when the MD simulations are repeated with non-native redox conditions, whereby only the terminal  $Fe_4S_4$  cluster (N2) is reduced (see SI Table S1), the hinge-bending motion is no longer observed in this chain. Clearly, the quinone-insertion path within complex I leverages the conformational transition of the soluble arm that results from the steady-state charge distribution of the  $Fe_4S_4$  clusters, with four clusters N3, N4, N6a, and N2 reduced.

Owing to the chemical nature of quinone, its reversible association with the protein complex requires concomitant accommodation of its polar headgroup and hydrophobic tail by the spatially elongated binding site. In the reduced complex I, Nqo4 residue Tyr87, central to the binding of the headgroup (see Figure 1 inset), remains in the vicinity of the terminal Fe<sub>4</sub>S<sub>4</sub> cluster N2. Nqo6 Arg83, listed as a switch residue in Figure 2C, also stays close to the N2 cluster when the latter is reduced. Therefore, when N2 is reduced, Tyr87 is stabilized by hydrogen-bonding to Arg83, opening the binding pocket.

Conversely, when N2 is oxidized, Arg83 moves away, breaking the hydrogen-bond with Tyr87 (see Figure S6). Tyr87 finds a new hydrogen-bonding partner in residue His38. This rearrangement of Tyr87 occludes the binding pocket, preventing entry of the quinone head. Stated differently, the conformation of the quinone binding pocket is redox-regulated by interactions with Arg83, which is a well-conserved residue in bacterial complex I.<sup>24</sup>

The elongated region of the binding pocket, which accommodates the quinone hydrophobic tail, however, only opens up when four  $\mathrm{Fe_4S_4}$  clusters are simultaneously reduced. When only the terminal  $\mathrm{Fe_4S_4}$  cluster is reduced, accommodation of the tail is thwarted by the absence of the hingebending motion within chain Nqo4. Taken together, the present simulations illuminate that the concerted dynamics of the soluble arm reflects local changes in the charge distribution of individual iron—sulfur clusters.

Reduced Complex I Favors Menaquinone Binding. We now consider a holo form of complex I, whereby a charge carrier is docked to its binding site, both for the oxidized and reduced states of the iron—sulfur clusters, and for the oxidized, i.e., menaquinone, and reduced, i.e., menaquinol, states of the substrate. From the simulations carried out at thermodynamic equilibrium, we measured the distance RMSD of each subunit of the soluble arm with respect to the initial structure (see Figure 4A). Although Nqo3 was by far the most dynamic subunit in apo complex I, irrespective of the oxidation state of the  $Fe_4S_4$  clusters, upon menaquinone binding, this subunit exhibits a much lesser mobility, as mirrored in the decrease of the distance RMSD by 2-3 Å (see Figure 4A).

Geometric free-energy calculations were performed to separate reversibly menaquinone from the protein complex. As can be seen in Figure 5B, the resulting potential of mean force (PMF) reveals the preferred location of the substrate

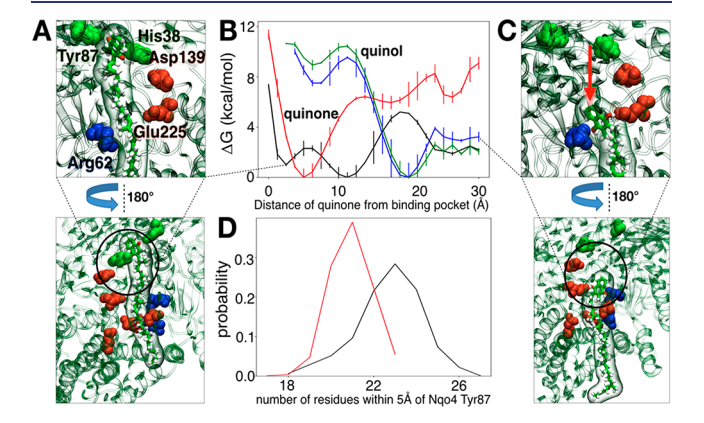


Figure 5. Free-energy profile of quinone-binding. (A) Snapshot of quinone near the binding pocket (green: binding pocket residues, red/blue: residues of the neck region, see later). (B) Free-energy profile of quinone/quinol-binding (black: quinone in oxidized complex I, red: quinone in reduced complex I, blue: quinol in oxidized complex I, green: quinol in reduced complex I). Quinone shows minima near the binding pocket (His38 and Tyr87 of Nqo4), while quinol minima is shifted ("neck" region). Location of quinone minima changes when complex I is reduced. (C) Snapshot of quinol near the neck region. (D) Distribution of the number of interacting partners of Tyr87 of Nqo4 (black: oxidized, red: reduced). List of residues are shown in Figure S9. Note that the zoomed-in views (top) of panels A and C have been rotated by 180° with respect to zoomed-out views (bottom) for clarity.

with respect to the binding site in an oxidized and reduced environment. When four of the seven Fe<sub>4</sub>S<sub>4</sub> clusters (N3, N4, N6a, N2) are reduced, the PMF exhibits a single, deep minimum at 4.5 Å, which corresponds to a binding mode whereby both His38 and Tyr87 are hydrogen-bonded to the headgroup. Moreover, association is facilitated by the broad access to the binding site, characteristic of the reduced apo state (see Figure 1 inset). Conversely, in the oxidized complex I, the same binding pocket is partially encumbered, precluding simultaneous interaction of the substrate with residues His38 and Tyr87, which results in a suboptimal association and higher, shifted free-energy minima. In this state, His38 and Tyr87 are, for the most part, hydrogen-bonded to each other (see Figure S7). The latter can be further explained by the formation of ancillary interactions of Tyr87 with neighboring residues in the oxidized complex I (see Figure 5D), at the expense of enthalpically favorable contacts with the charge carrier. It is worth noting that beyond 6 Å, the free-energy increases sharply in the reduced complex I, but decreases in the oxidized form, owing to favorable hydrophobic interactions promoted by tighter contacts of the quinone tail with the protein.

In stark contrast with the oxidized reactant, menaquinone form of the charge carrier, the reduced product, menaquinol form interacts with the protein following a markedly different binding mode. Illustrated in Figure 5C as the "neck" region, the two hydroxyl groups are concomitantly hydrogen-bonded to the carboxylate moiety of residues Nqo8 Glu225 and Nqo3 Glu248. This alternate interaction pattern (detailed in Figure S8) is reflected in a sharp minimum of the PMF, shifted from that of menaquinone by ca. 6 Å, irrespective of the redox state of the iron-sulfur clusters. In addition, the reduced complex has a more open cavity than the oxidized one; hence, the steric hindrance experienced by the quinol is expected to diminish, which, in turn, leads to a shallow free-energy profile between 6 and 10 Å from the binding pocket. The discrepant free-energy profiles obtained for menaquinone and menaquinol suggest a dynamic adaptation of the binding pocket in response to the redox state of the substrate for facilitating quinol release.

The large free-energy barrier that separates the two minima for menaquinone when the  $Fe_4S_4$  clusters are reduced is indicative of a millisecond-scale residence time of the substrate at the binding site, which can be estimated, using the Szabo-Schulten equation, <sup>26</sup>

$$\tau = \int_{\xi_{\mathrm{A}}}^{\xi_{\mathrm{B}}} \mathrm{d}\xi \frac{\int_{\xi_{\mathrm{A}}}^{\xi} \mathrm{d}\xi' \exp(-\beta w(\xi'))}{D(\xi) \exp(-\beta w(\xi))}$$

where  $w(\xi)$  is the PMF,  $D(\xi)$  is the position-dependent diffusivity, and  $\beta=(k_{\rm B}T)^{-1}$ , with  $k_{\rm B}$ , the Boltzmann constant, and T, the temperature. Diffusivity of ubiquinone in a lipid environment has been measured experimentally  $^{27,28}$  to be  $5\times 10^{-8}$  cm $^2/{\rm s}$ . We employed the Green–Kubo relationship to determine the position-dependent diffusion coefficient of menaquinone (Figure S10), and the values are found to be roughly an order of magnitude larger, indicating faster diffusion. We also find in Figure S10 that the diffusion coefficient changes moderately with respect to the quinone position. Integration of this position-dependent diffusion coefficient with the PMF in the framework of the Szabo-Schulten equation  $^{26}$  yields an estimate of the mean first passage time for quinone binding and unbinding. The bounds of the integral were chosen based on features in the PMFs: A

corresponds to the closest free-energy minimum from the quinone-binding pocket, and B to the farthest minimum from it

Quinone-headgroup access to the binding site is fast, taking about 11 us; this value is computed again using the Szabo-Schulten equation, but now integrating the PMF in the direction of ligand entry, i.e., from higher to lower values of the distance from the quinone binding pocket, where the kinetic barriers are lower. Quinone-exit is relatively slow, spanning 0.5 s, ensuring that the charge carrier can stay bound until it is reduced. However, since the carrier needs only picoseconds to be reduced, 13,15 such a long-lived quinone-bound state is potentially precluded under turnover. Upon reduction, the quinol headgroup exits from the binding site at a rate much faster than that of quinone entry. Nevertheless, the fast exit is followed by entrapment of the quinol head in the neck region of the binding pocket (see Figure 5C), resulting in an energy barrier of 4 kcal/mol. This barrier arises from overcoming the hydrogen-bond interactions of the quinol and Nqo8 Glu225 and Nqo8 Glu248. We determine quinol-exit from the neck region to be the slowest step in menaquinone entry/exit process, taking about 2.4 ms, in the ballpark of the experimentally measured turnover time of about 5 ms.<sup>21</sup> In mammals, it has been shown that ubiquinol-tail length has minimal impact on the rate of complex I turnover.<sup>29</sup> agreement with this finding, it is indeed the reduced menaquinone headgroup (and not tail) that contributes to the energy bottleneck.

Menaquinone versus Ubiquinone Binding. Some recent publications 12,30 have reported the free-energy of quinone binding to complex I. There are three major differences between these investigations and the current work. First, we studied the more biologically relevant menaquinone native to T. thermophilus, which includes a bulkier aromatic ring, absent in the ubiquinone. Second, instead of using short-tailed Q1 in free-energy calculations to avoid sampling the slow movements of a long quinone tail, we used throughout the complete 40-carbon (8 isoprenyl units), menaquinone/menaquinol. Third, unlike the work reported by those and other authors,  $^{12,14,30}$  where only one Fe<sub>4</sub>S<sub>4</sub> cluster was reduced, we monitored quinone-binding when half of the eight conserved Fe-S (6 Fe<sub>4</sub>S<sub>4</sub> and 2 Fe<sub>2</sub>S<sub>2</sub>) clusters were reduced, following EPR/DEER/Mössbauer data (Figure 4B). <sup>17,19,23</sup> These three key differences in the elaboration of the models translate into dramatic changes in the free-energy landscape, and, therefore, in the physical interpretation of quinone binding.

The menaquinone free-energy profiles in this work show clear differences from that of ubiquinone (10 isoprenyl units) reported previously. 12,30 For a bound menaquinone, the global minimum is shifted to 5 Å, much closer to the locus of the binding site, compared to the 35 Å minimum of ubiquinone. Thus, our model indicates that the transfer of menaquinone into the site of reduction is more spontaneous than that of ubiquinone—a possible design advantage making menaquinone the physiological substrate in *T. thermophilus*. Disparities between menaquinone and ubiquinone binding have already been observed in complex II.<sup>31</sup> We have further analyzed how some of the residues stabilizing ubiquinone while entering the binding pocket cannot be accessed by the bulkier menaquinone (Figure S11). For example, menaquinone does not interact with the secondary binding pocket, comprising residues Trp37 (Nqo6), Arg62 (Nqo6), and Arg36 (Nqo8),

unlike ubiquinone in previous studies.<sup>12</sup> Thus, a potentially deep intermediate binding pocket on the way to the final reaction site is avoided by menaquinone, leading instead to a local minimum at that position. The detailed mechanism of quinone binding established in our study is at variance with that of Warnau et al.,<sup>12</sup> and possibly more biologically relevant, as we show how access to the reaction site is energetically favored. Altogether, our simulations offer unforeseen insight at the cross-section of redox-induced protein conformational changes and their varied impact on binding charge carriers of different geometry.

**Mutations in Complex I.** As summarized in Figure 6, we have identified three categories of residues in complex I based

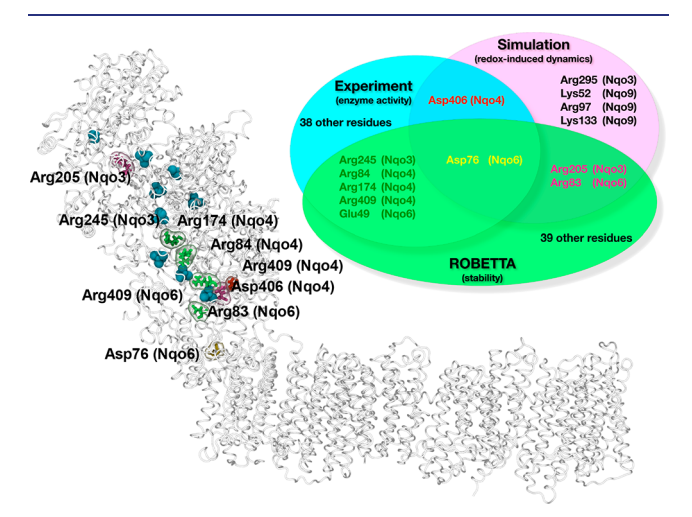


**Figure 6.** Comparison of complex I simulation with experimental results. Three categories of residues are shown as a Venn diagram (inset), and their locations on complex I are shown in the adjacent part. Residues that affect function by stabilizing or destabilizing subunit—subunit interfaces are highlighted in green. Residues that affect function through redox-induced dynamics are highlighted in red. Asp 76 (Nqo6), the unique residue that affects function through stability as well as redox-sensitivity, is highlighted in yellow. Highlighted in pink are the residues that affect stability and redox motion but are heretofore not known to be functionally active. Iron—sulfur clusters are shown in blue for reference.

on whether or not they affect (i) interface stability, (ii) redoxinduced dynamics, and (iii) enzyme activity. ROSETTA alanine scanning<sup>32,33</sup> of the residues at the interface of the soluble subunits revealed 47 residues with  $|\Delta \Delta G| > 0.6$  kcal/ mol, implying significant changes in stability. Three out of these 47 residues, namely, Asp76 (Nqo6), Arg205 (Nqo3), and Arg83 (Nqo6), were also found to be redox-sensitive in our simulations (Figure 2E). Therefore, we predict that these residues have dual functions-maintaining complex I stability as well as mediating mechanical motion in response to Fe<sub>4</sub>S<sub>4</sub> reduction. Residue Asp 406 (Nqo4) was also found to be redox-sensitive in Figure 2E. An alanine mutation of this residue has minimal impact on the stability of the complex (see Table S3); yet, such replacement is known to reduce complex I activity to 20%.34 Thus, the redox-sensitive residues identified in our simulations, indeed control enzyme activity notwithstanding their contribution to interface stability.

Next, we look into the sites of complex I mutations that are essential for enzyme activity. A list of such mutations, along with their corresponding sites in *T. thermophilus* has already been published. Comparison of these mutation sites with our

ROSETTA predictions confirmed six residues, namely, Arg245 (Nqo3), Arg84 (Nqo3), Arg174 (Nqo6), Glu49 (Nqo6), Arg409 (Nqo6), and Asp76 (Nqo6), that contribute to complex I stability (see Table S3). Remarkably, we find that mutations of two out eight of these residues (Arg245 and Arg174) are implicated in human diseases. Therefore, our combined MD-ROSETTA analysis detects specific residues that correlate reduced complex I stability with potential enzyme malfunctions.

Finally, we seek residues that control all the three biochemical effects. Upon  $Fe_4S_4$  reduction, Asp76~(Nqo6) undergoes significant conformational transition (Figure 2E) to move away from the reduced cluster (N2) by  $\sim 24~\text{Å}$ . An alanine mutation of this residue overstabilizes the interface by 0.75 kcal/mol (see Table S3) and reduces the activity to only  $6\%.^{37}$  Therefore, we discover that Asp76 is unique in that it comodulates stability with redox-induced dynamics and enzyme activity. We note that the aforementioned Arg205 (Nqo3) and Arg83 (Nqo6) residues affect both stability and redox-driven motions, strongly suggesting a functional role. On the basis of these findings, we suggest these two locations for future mutation studies.

Menaquinone-Binding Allows Hydrogen-Bonded Networks in the E-Channel. Having been established through our simulations the dynamics between the soluble arm of complex I and its quinone binding site, we now focus on the TM region of the protein complex, notably on the first of the four water channels, referred to as E-channel. Crystallographic studies implicate glutamate residues 130, 163, and 248 of subunit Nqo8, and aspartate residue 72 of subunit Nqo7 in pumping protons across the membrane. Such transport is possible only if there is a network of water-mediated hydrogen-bonds connecting these residues. The number of water-peptide hydrogen bonds in the presence and absence of the bound menaquinone is presented in Figure 7C,D. In the absence of menaquinone, there is a drastic reduction in the probability of water-mediated hydrogen-

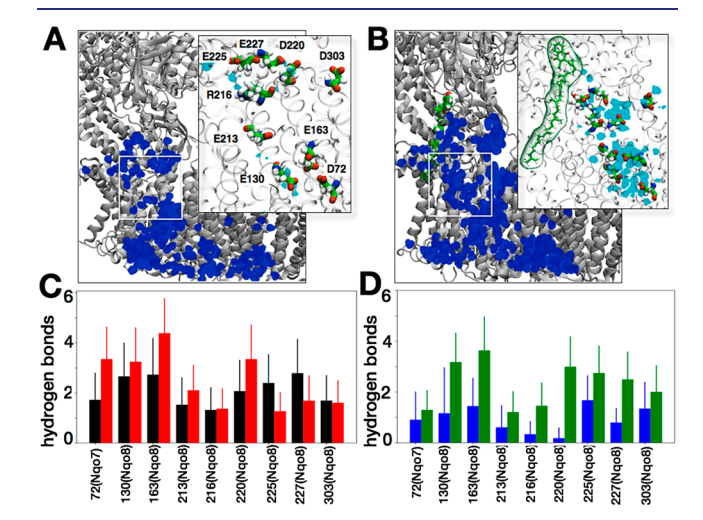


Figure 7. Solvation of the TM region within (A) apo and (B) menaquinone-bound complex I. Water-mediated hydrogen-bond networks are shown in insets. A strong hydrogen-bonded network is seen upon quinone-binding which is missing in apo complex I. Average and standard deviation of the number of hydrogen-bonds between these residues and water is shown for both the oxidized (C) and reduced (D) complex I in apo (black and blue) and quinone-bound (red and green) states.

bonds. The differences in the water occupancy between these two states are even more glaring when complex I is reduced. In the absence of a bound quinone, water access is reduced 3- to 4-fold for key residues connected to the quinone binding pocket, hindering proton transport in the reduced complex. This analysis indicates that in the apo state of complex I, the hydrogen-bond network is sparser than that characteristic of the menaquinone-bound state. In other words, the menaquinone-bound structure promotes proton-pumping in the Echannel, thereby establishing the role played by the charge carrier in the chemo-mechanical coupling between the hydrophilic and membrane arms of the complex, as well as the necessity of quinone binding for proton transport.

## CONCLUSIONS

In this contribution, we have examined the response of the hydrophilic arm of respiratory complex I to redox variations and its impact on the quinone binding and the TM domain conformation. Toward this end, distinct computational assays have been designed, whereby four out of seven Fe<sub>4</sub>S<sub>4</sub> clusters in the main redox chain are in a reduced state, and compared with configurations wherein either only the terminal ironsulfur cluster is reduced, or all of them are in an oxidized state. The reduced complex I promotes menaquinone binding, in sharp contrast with the oxidized form. Specifically, isomerization of key basic residues in response to the redox state of the iron-sulfur clusters loosens protein-protein interfaces, opening allosterically the quinone binding site. The binding pose involving the reduced form of the charge carrier, i.e., menaquinol, is significantly different from that of the oxidized form, i.e., menaquinone, which penetrates deeper in the subunit Nqo4, resulting in a sharp minimum of the free-energy landscape. This position of menaguinone close to the Fe<sub>4</sub>S<sub>4</sub> cluster N2 is essential for effective electron transfer. Accordingly, quinol exit-upon quinone reduction and protonation—is thermodynamically favored, irrespective of the redox state of the protein complex. This final step is necessary in the catalytic cycle, so that quinol can be exchanged for a new molecule of quinone. Even though previous investigations have reported short-time scale (ps) charge-transfer processes involving differences between the two quinone species, 13,15 our work offers first insights into the ms-time scale dynamics of ubiquinone vs menaquinone binding to redox-coupled conformations of complex I. The difference in quinone motions clearly shows why menaquinone is preferred over ubiquinone by *T. thermophilus*.

We find that menaquinone turnover takes only microseconds while its release takes approximately 2.4 ms. This time scale is slower than that of plastoquinone turnover by the photosystem II, <sup>38</sup> yet faster than ubiquinone turnover by purple bacteria complex III. <sup>39</sup> It is useful to keep complex I moving at the millisecond time scale, so that conformational coupling for the generation of the proton motive force by its transmembrane domains can occur over time intervals comparable to the frequency of ATP synthesis. A faster turnover might lead to excess proton gradient across the membrane and proton leak. <sup>40</sup>

It has been shown computationally that cardiolipins transiently bind to the transmembrane regions of mammalian complex I and induce global conformational changes, which improve the quinone accessibility of the binding pocket. A very similar result was also obtained for complex III. Furthermore, lack of binding of the quinones in the absence

of cardiolipins in the membrane has previously been observed. Analogous to the aforementioned results, introduction of cardiolipins in the model membrane might be expected to enhance quinone binding even further in reduced complex I. However, the membrane in *T. thermophilus* is primarily composed of glycolipid, glycophospholipid, and carotenoids; rarely have cardiolipins been observed or simulated. To the best of our knowledge, all existing studies of ubiquinone binding to complex I in *T. thermophilus* have been performed in POPC membranes, 12,30 as is ours. Atomistic or coarse-grained simulations of complex I in a more realistic membrane is expected to have biologically relevant ramifications. 44

The chemical details derived from our simulations allow known complex I mutations to be clustered in three different classes: stabilizing/destabilizing, redox-sensitive, functionally relevant. Our predicted mutations that line the boundaries of two to three of such classes can now be tested experimentally to tune the efficiency of complex I functions. Quinone binding is coupled to proton pumping through the formation of concerted, through-space hydrogen-bond networks involving chains of water molecules. Conversely, in the apo state of complex I, such a network is less probable, and so is potentially proton pumping, or leakage, across the mitochondrial membrane. Altogether, the present work establishes basic design principles of respiratory complex I, starting from the electron input into FMN, followed by the reduction of the Fe<sub>4</sub>S<sub>4</sub> redox chain, and eventual reduction and protonation of the quinone. These events are linked to a clear change in the pattern of polar interactions within the membrane arm, in the vicinity of the quinone. How these processes lead to proton translocation in the distal antiporter-like subunits remains an open question and a subject for future work.

## ■ METHODS

**Molecular Assays.** The initial molecular assay was built using the 3.3 Å crystal structure of the entire respiratory complex I of T. themophilus (pdb: 4HEA, with loop Nqo6 55–70 updated as in the structure with decyl-ubiquinone bound [PDB 6Y11], to be published separately). The 16 subunits of the quaternary assembly together with the nine iron–sulfur clusters and the flavin mononucleotide were all included in the model. Structure of missing residues of subunits Nqo3 (56–72, 114–147, and 778–783) was inferred using the automodel class of Modeler. The protonation state of titratable residues was assigned based on  $pK_a$  values predicted by PropKa. The results were comparable to Luca et al.,  $^{14}$  as reported in Table S1.

For histidines, the protonation state of imidazole ring nitrogens (proton on either  $\varepsilon$  or  $\delta$  nitrogens, or on both) was chosen based on the local chemical environment and the capacity to form hydrogen bonds. We are aware that His169 is a so-called redox Bohr group. ^13,45,46 We have attributed the protonation state of this group according to the hydrogen-bond optimization allowed within the surrounding electrostatic environment, using the software ProPka. In addition, we based our choice of protonation states based on the recent QM work by Gamiz-Hernandez et al., who predict histidine to be deprotonated due to reduction of N2. ^13 The oxidized state can also be modeled as protonated in light of the Monte Carlo simulation of Couch et al. ^7 In contrast with Brandt and co-workers, Couch et al. concluded, however, that "His-169 is protonated in both the reduced and oxidized enzyme in this pH range." Therefore, we have modeled the reduced complex with deprotonated His, and the oxidized complex with protonated His.

The Dowser program was used to fill empty cavities by water within the complex transmembrane region, resulting in the addition of 121 water molecules. The molecular system was subsequently embedded in a hydrated patch of 1000 1-palmitoyl-2-oleoyl-sn-

glycero-3-phosphocholines (POPC) in the presence of 150 mM of NaCl. The complete molecular assay consists of ~1 000 000 atoms embedded in a rectangular box of 28 × 14 × 24 nm<sup>3</sup>. Complex I subunits, lipids, and ions were described with the CHARMM36 force field including CMAP corrections for proteins. The TIP3P model was employed to describe water. The iron-sulfur (Fe-S) cluster CHARMM-like parameters were those derived by Chang and Kim from Density Function Theory calculations. 48 The flavin mononucleotide was described with the parameter set designed by Freddolino et al. 49 All the Fe-S clusters are modeled as oxidized in the oxidized complex I. In the reduced state, clusters N3, N4, N6a, and N2 are modeled as reduced. The other four clusters, namely N1a, N1b, N5, and N6b are unlikely to be reduced under steady-state turnover, as demonstrated for bovine complex I. 17,19,23 E. coli complex I is unique because it has a high-potential NADH-reducible cluster N1a. This uniqueness manifests itself in a different steady state, wherein the N1a, N1b, N6a, and N2 clusters are reduced. 50 The clusters of *T. thermophilus* complex I are not characterized at the same level of detail as those of E. coli, yet it is conclusively shown that N1a is not NADH-reducible, akin to bovine complex I.51,52 We have, therefore, modeled the Fe-S clusters in T. thermophilus following the pattern of bovine complex I (rather than that of E. coli). In line with the existing literature on the redox biochemistry of Fe-S clusters in respiratory complexes,<sup>8</sup> the combination that we used is in all likelihood the most probable in vivo.

**Quinone Docking.** The polar ring of menaquinone was aligned with that of decyl-ubiquinone in the X-ray structure (PDB ID: 6Y11), so the phenyl oxygens are interacting with residues His 38 and Tyr 87 of subunit Nqo4. The menaquinone tail was then refined using 10 ns of Molecular Dynamics Flexible Fitting (MDFF)<sup>53</sup> simulations into the hollow quinone-binding cavity. The structure with the highest cross-correlation and lowest energy was chosen for subsequent MD simulation.

**Simulation Details.** The system was equilibrated in the NPT ensemble ( $T=313~\rm K$ ,  $P=1~\rm atm$  for 100 ns before initiating production runs. Simulations were performed using 1.0 fs time step with a force-based switching function for long-range interactions from 10 to 12 Å, Langevin thermostat, Nosé—Hoover Langevin barostat, and a flexible cell. List of simulation systems along with system size, box size, simulation length, and number of repetitions is provided in Table S2. A total of 10  $\mu$ s conventional MD is performed.

Free Energy Calculations. To accelerate the unbinding of the menaquinone (microseconds to milliseconds) to time scales that are accessible for MD simulations (nanoseconds), the method of steered molecular dynamics (SMD) is used.<sup>54</sup> Here, a moving harmonic constraint is added to the potential energy function to apply an external force to the ubiquinone molecule. In our simulations, a constant-velocity scheme was used with a pulling speed of 10 Å/ns and a spring constant for the harmonic constraint of 500 pN/Å. This ensures that the system closely follows the pulling potential and the stiff spring approximation can be applied. Following the procedure used by Aird et al.,<sup>54</sup> the main focus was on the headgroup. It represents the most voluminous part of the menaquinone molecule and therefore has the largest effect on the simulation results. The atom chosen for attaching the moving constraint was the carbon atom of the last isoprenoid unit of the ubiquinone tail. By pulling the menaquinone molecule only on the tail atom, the headgroup of the menaquinone is almost free to move and can therefore find a lowenergy pathway through complex I's quinone-access channel (Figure

Pulling in both directions was done to gain information on the potential pathway from independent simulations. The system was prepared in an orientation such that the x axis was parallel to the direction connecting the center of the binding pocket (residues 38 and 87 of subunit Nqo4) with the channel opening (Figure S12), and the z axis was parallel to the membrane normal. The SMD direction was parallel to the membrane plane along the positive x-direction. The pulling distance was  $\sim$ 12 Å, which resulted in a total simulation time of ca. 250 ns. Four such pulling simulations were performed for

systems (oxidized or reduced complex I, bound to quinone or quinol), cumulatively taking 1  $\mu$ s.

To reconstruct the potential of mean force (PMF) along the proposed pathway, Bias-exchange umbrella sampling (BEUS) simulations were performed along the path derived from the SMD trajectories of oxidized or reduced menaquinone unbinding. Details of these steering simulation have been published separately.<sup>25</sup> The BEUS simulations for the four pathways are performed employing the distance of quinone headgroup from the binding pocket as the collective variable, as also used by others. <sup>12</sup> To ensure sufficient window overlap in BEUS simulations, 34 windows were employed along the dissociation path. An exchange is attempted every 1 ps between each image and one of its two nearest neighboring images in an alternating fashion. Ten replicas per image are employed for 5 nslong BEUS simulations. A force constant of 5 kcal/mol/ Å<sup>2</sup> is employed to geometrically restrain the position of the umbrellas along the interheme distance axis. This protocol resulted in a roughly similar rate of exchange between neighboring windows (ranging from 22% to 30%, Figure S13). Cumulatively, 4 × 5 ns/replica × 10-replica/ window  $\times$  34 windows = 6.8  $\mu$ s of BEUS simulations were performed for the construction of four one-dimensional free-energy profiles. Thus, an aggregate of 10  $\mu$ s conventional MD + 1  $\mu$ s SMD + 6.8  $\mu$ s of BEUS =  $17.8 \mu s$  simulations were performed.

Thereafter our generalized weighted histogram methodology<sup>55</sup> was employed to reweight the ensemble and determine the potential of mean force (PMF) profiles (Figures 5 and S13). Convergence of the free-energy calculation is tested for each of the three cases using a resampling protocol. 50% of the data are randomly chosen and two one-dimensional free energy profiles are constructed employing the aforementioned weighted histogram method. The process is repeated 200 times to obtain a collection of 200 PMFs. After these 200 trials a converged mean profile is obtained across the 200 PMFs, and the standard deviation is considered as the error estimate (Figure 5B).

Diffusivity Calculations. A swarm of ten unbiased MD trajectories was launched starting with the lowest energy model from the umbrella sampling windows, after sorting the constrained ensembles. Each trajectory was run for 1 ps, and the swarms were collected for ten evenly spaced windows out of the 30 used in BEUS, sampling distinct locations of the menaquinone or menaquinol. Similar to BEUS, we monitored the distance of quinone headgroup from the binding pocket. Velocity autocorrelation functions were measured for this distance form each replica within a swarm, and averaged over the ten replicas. Thus, ten velocity autocorrelation profiles were determined at different locations of the quinone within the pocket. The area under these profiles was computed to estimate the position-dependent diffusion coefficient.

**Analysis Details.** Subunit rotation (change in principal component direction) was calculated by subtracting the angle of the principal components with respect to Z-axis in the final structure from the initial structure (initial structure was the crystal structure for aposimulations. For quinone-bound simulations, it was the structure obtained after docking the quinone to the crystal structure). Principal components were calculated by VMD's draw principal axes tool.

Intersubunit contact surface area between subunits A and B ( $CS_{AB}$ ) was calculated by the following equation:

$$CS_{AB} = S_A + S_B - S_{AB}$$

where  $S_X$  is the solvent-accessible surface area (SASA) of subunit X ( $S_{AB}$  is the SASA of subunits A and B taken together), which were calculated by VMD's measure sasa tool using a probe radius of 1.4 Å. Electrostatic potentials were calculated using VMD's PMEpot plugin. Network analysis of correlated motion of different regions was performed by Dynamic Network Analysis tool of VMD. Hydrogen bonds were detected by VMD's hbonds plugin using a donor–acceptor distance cutoff of 3.0 Å and donor-proton-acceptor angle cutoff of  $20^\circ$ .

In line with standard practices in free-energy calculations, <sup>56</sup> we have employed the Szabo-Schulten equation <sup>26</sup> to recover longer time scale information from our s-long simulations. Under the assumption of adiabatic time separation, inference of longer-time trends is

possible.<sup>26,57</sup> Diffusive nature of the quinone motion is illustrated in Figure S10 employing the Green–Kubo relationship.

ROBETTA alanine scanning was performed on the residues lining the interfaces of the soluble subunits of complex I (Table S3). In this, residues are computationally mutated to an alanine, and the accompanying change in free energy ( $\Delta\Delta G$ ) is calculated by a Monte Carlo-based algorithm.

The software used in this work is listed in Table S4.

#### ASSOCIATED CONTENT

### Supporting Information

The Supporting Information is available free of charge at https://pubs.acs.org/doi/10.1021/jacs.9b13450.

Additional analyses of the trajectories (PDF) Movies (ZIP)

#### AUTHOR INFORMATION

#### **Corresponding Authors**

Christophe Chipot — Department of Physics, University of Illinois at Urbana—Champaign, Urbana, Illinois 61801, United States; University of Lorraine, Nancy 54000, France; orcid.org/0000-0002-9122-1698;

Email: christophe.chipot@univ-lorraine.fr

Leonid Sazanov — Institute of Science and Technology, 3400 Klosterneuburg, Austria; Email: sazanov@ist.ac.at

Abhishek Singharoy — School of Molecular Sciences and Biodesign Institute, Arizona State University, Tempe, Arizona 85281, United States; orcid.org/0000-0002-9000-2397; Email: asinghar@asu.edu

#### **Authors**

Chitrak Gupta — School of Molecular Sciences and Biodesign Institute, Arizona State University, Tempe, Arizona 85281, United States

Umesh Khaniya — Department of Physics, City College of New York, New York, New York 10031, United States; Department of Physics, City University of New York, New York, New York 10017, United States

Chun Kit Chan — Department of Physics, University of Illinois at Urbana—Champaign, Urbana, Illinois 61801, United States Francois Dehez — University of Lorraine, Nancy 54000, France; orcid.org/0000-0001-8076-6222

Mrinal Shekhar — Department of Physics, University of Illinois at Urbana—Champaign, Urbana, Illinois 61801, United States

M. R. Gunner — Department of Physics, City College of New York, New York, New York 10031, United States; Department of Physics, City University of New York, New York, New York 10017, United States

Complete contact information is available at: https://pubs.acs.org/10.1021/jacs.9b13450

## Notes

The authors declare no competing financial interest.

#### ACKNOWLEDGMENTS

A.S. and C.G. acknowledge start-up funds from the SMS and CASD at Arizona State University, and the resources of the OLCF at the Oak Ridge National Laboratory, which is supported by the Office of Science at DOE under Contract No. DE-AC05-00OR22725, made available via the INCITE program. A.S. acknowledges CAREER award from NSF (MCB-1942763) and MCB-1616590. C.C. and F.D. are grateful to the Contrat Plan État Région (CPER) IT2MP

and to the Fonds Européen de Développement en Région (FEDER) for generous funding. M.G. and U.K. acknowledge funding from the National Science Foundation (grant number MCB-1519640).

#### REFERENCES

- (1) Formosa, L. E.; Ryan, M. T. Mitochondrial OXPHOS Complex Assembly Lines. *Nat. Cell Biol.* **2018**, 20 (5), 511–513.
- (2) Sazanov, L. A. A Giant Molecular Proton Pump: Structure and Mechanism of Respiratory Complex I. *Nat. Rev. Mol. Cell Biol.* **2015**, 16 (6), 375–388.
- (3) Baradaran, R.; Berrisford, J. M.; Minhas, G. S.; Sazanov, L. A. Crystal Structure of the Entire Respiratory Complex I. *Nature* **2013**, 494 (7438), 443–448.
- (4) Fiedorczuk, K.; Letts, J. A.; Degliesposti, G.; Kaszuba, K.; Skehel, M.; Sazanov, L. A. Atomic Structure of the Entire Mammalian Mitochondrial Complex I. *Nature* **2016**, *538* (7625), 406–410.
- (5) Yoshida, M.; Muneyuki, E.; Hisabori, T. ATP Synthase a Marvellous Rotary Engine of the Cell. *Nat. Rev. Mol. Cell Biol.* **2001**, 2 (9), 669–677.
- (6) Watt, I. N.; Montgomery, M. G.; Runswick, M. J.; Leslie, A. G. W.; Walker, J. E. Bioenergetic Cost of Making an Adenosine Triphosphate Molecule in Animal Mitochondria. *Proc. Natl. Acad. Sci. U. S. A.* **2010**, *107* (39), 16823–16827.
- (7) Moser, C. C.; Farid, T. A.; Chobot, S. E.; Dutton, P. L. Electron Tunneling Chains of Mitochondria. *Biochim. Biophys. Acta, Bioenerg.* **2006**, 1757 (9), 1096–1109.
- (8) Hirst, J. Mitochondrial Complex I. *Annu. Rev. Biochem.* **2013**, 82 (1), 551–575.
- (9) Sazanov, L. A. Respiratory Complex I: Mechanistic and Structural Insights Provided by the Crystal Structure of the Hydrophilic Domain. *Biochemistry* **2007**, 46 (9), 2275–2288.
- (10) Hirst, J. Towards the Molecular Mechanism of Respiratory Complex I. *Biochem. J.* **2010**, 425 (2), 327–339.
- (11) Jussupow, A.; Di Luca, A.; Kaila, V. R. I. How Cardiolipin Modulates the Dynamics of Respiratory Complex I. *Sci. Adv.* **2019**, *5* (3), No. eaav1850.
- (12) Warnau, J.; Sharma, V.; Gamiz-Hernandez, A. P.; Di Luca, A.; Haapanen, O.; Vattulainen, I.; Wikstrom, M.; Hummer, G.; Kaila, V. R. I. Redox-Coupled Quinone Dynamics in the Respiratory Complex I. *Proc. Natl. Acad. Sci. U. S. A.* **2018**, *115* (36), E8413–E8420.
- (13) Gamiz-Hernandez, A. P.; Jussupow, A.; Johansson, M. P.; Kaila, V. R. I. Terminal Electron—Proton Transfer Dynamics in the Quinone Reduction of Respiratory Complex I. J. Am. Chem. Soc. 2017, 139 (45), 16282—16288.
- (14) Di Luca, A.; Gamiz-Hernandez, A. P.; Kaila, V. R. I. Symmetry-Related Proton Transfer Pathways in Respiratory Complex I. *Proc. Natl. Acad. Sci. U. S. A.* **2017**, *114* (31), E6314–E6321.
- (15) Saura, P.; Kaila, V. R. I. Energetics and Dynamics of Proton-Coupled Electron Transfer in the NADH/FMN Site of Respiratory Complex I. J. Am. Chem. Soc. 2019, 141 (14), 5710–5719.
- (16) Hirst, J.; Roessler, M. M. Energy Conversion, Redox Catalysis and Generation of Reactive Oxygen Species by Respiratory Complex I. *Biochim. Biophys. Acta, Bioenerg.* **2016**, *1857* (7), 872–883.
- (17) Verkhovskaya, M. L.; Belevich, N.; Euro, L.; Wikström, M.; Verkhovsky, M. I. Real-Time Electron Transfer in Respiratory Complex I. *Proc. Natl. Acad. Sci. U. S. A.* **2008**, *105* (10), 3763–3767.
- (18) Verkhovskaya, M.; Bloch, D. A. Energy-Converting Respiratory Complex I: On the Way to the Molecular Mechanism of the Proton Pump. *Int. J. Biochem. Cell Biol.* **2013**, *45* (2), 491–511.
- (19) Bridges, H. R.; Bill, E.; Hirst, J. Mössbauer Spectroscopy on Respiratory Complex I: The Iron–Sulfur Cluster Ensemble in the NADH-Reduced Enzyme Is Partially Oxidized. *Biochemistry* **2012**, *51* (1), 149–158.
- (20) Page, C. C.; Moser, C. C.; Chen, X.; Dutton, P. L. Natural Engineering Principles of Electron Tunnelling in Biological Oxidation—Reduction. *Nature* **1999**, 402 (6757), 47–52.

- (21) Vinogradov, A. D. Catalytic Properties of the Mitochondrial NADH—Ubiquinone Oxidoreductase (Complex I) and the Pseudo-Reversible Active/Inactive Enzyme Transition. *Biochim. Biophys. Acta, Bioenerg.* **1998**, *1364* (2), 169—185.
- (22) Zickermann, V.; Wirth, C.; Nasiri, H.; Siegmund, K.; Schwalbe, H.; Hunte, C.; Brandt, U. Mechanistic Insight from the Crystal Structure of Mitochondrial Complex I. *Science* **2015**, 347 (6217), 44–49.
- (23) Roessler, M. M.; King, M. S.; Robinson, A. J.; Armstrong, F. A.; Harmer, J.; Hirst, J. Direct Assignment of EPR Spectra to Structurally Defined Iron-Sulfur Clusters in Complex I by Double Electron—Electron Resonance. *Proc. Natl. Acad. Sci. U. S. A.* **2010**, *107* (5), 1930—1935
- (24) Berrisford, J. M.; Sazanov, L. A. Structural Basis for the Mechanism of Respiratory Complex I. J. Biol. Chem. 2009, 284 (43), 29773–29783.
- (25) Singharoy, A.; Barragan, A. M.; Thangapandian, S.; Tajkhorshid, E.; Schulten, K. Binding Site Recognition and Docking Dynamics of a Single Electron Transport Protein: Cytochrome C2. J. Am. Chem. Soc. 2016, 138 (37), 12077–12089.
- (26) Szabo, A.; Schulten, K.; Schulten, Z. First Passage Time Approach to Diffusion Controlled Reactions. *J. Chem. Phys.* **1980**, 72 (8), 4350–4357.
- (27) Di Bernardo, S.; Fato, R.; Casadio, R.; Fariselli, P.; Lenaz, G. A High Diffusion Coefficient for Coenzyme Q10 Might Be Related to a Folded Structure. FEBS Lett. 1998, 426 (1), 77–80.
- (28) Marchal, D.; Boireau, W.; Laval, J. M.; Moiroux, J.; Bourdillon, C. Electrochemical Measurement of Lateral Diffusion Coefficients of Ubiquinones and Plastoquinones of Various Isoprenoid Chain Lengths Incorporated in Model Bilayers. *Biophys. J.* **1998**, 74 (4), 1937–1948.
- (29) Fedor, J. G.; Jones, A. J. Y.; Di Luca, A.; Kaila, V. R. I.; Hirst, J. Correlating Kinetic and Structural Data on Ubiquinone Binding and Reduction by Respiratory Complex I. *Proc. Natl. Acad. Sci. U. S. A.* **2017**, *114* (48), 12737–12742.
- (30) Hoias Teixeira, M.; Menegon Arantes, G. Balanced Internal Hydration Discriminates Substrate Binding to Respiratory Complex I. *Biochim. Biophys. Biochim. Biophys. Acta, Bioenerg.* **2019**, *1860* (7), 541–548.
- (31) Maklashina, E.; Cecchini, G. The Quinone-Binding and Catalytic Site of Complex II. *Biochim. Biophys. Acta, Bioenerg.* **2010**, 1797 (12), 1877–1882.
- (32) Kortemme, T.; Baker, D. A Simple Physical Model for Binding Energy Hot Spots in Protein—Protein Complexes. *Proc. Natl. Acad. Sci. U. S. A.* **2002**, 99 (22), 14116—14121.
- (33) Kortemme, T.; Kim, D. E.; Baker, D. Computational Alanine Scanning of Protein-Protein Interfaces. *Sci. Signaling* **2004**, 2004 (219), pl2–pl2.
- (34) Kashani-Poor, N.; Zwicker, K.; Kerscher, S.; Brandt, U. A Central Functional Role for the 49-KDa Subunit within the Catalytic Core of Mitochondrial Complex I. *J. Biol. Chem.* **2001**, 276 (26), 24082–24087.
- (35) Duarte, M.; Schulte, U.; Ushakova, A. V.; Videira, A. Neurospora Strains Harboring Mitochondrial Disease-Associated Mutations in Iron-Sulfur Subunits of Complex I. *Genetics* **2005**, *171* (1), 91–99.
- (36) Kerscher, S.; Grgic, L.; Garofano, A.; Brandt, U. Application of the Yeast Yarrowia Lipolytica as a Model to Analyse Human Pathogenic Mutations in Mitochondrial Complex I (NADH:Ubiquinone Oxidoreductase). *Biochim. Biophys. Acta, Bioenerg.* **2004**, *16*59 (2), 197–205.
- (37) Garofano, A.; Zwicker, K.; Kerscher, S.; Okun, P.; Brandt, U. Two Aspartic Acid Residues in the PSST-Homologous NUKM Subunit of Complex I from Yarrowia Lipolytica Are Essential for Catalytic Activity. *J. Biol. Chem.* **2003**, 278 (43), 42435–42440.
- (38) Van Eerden, F. J.; Melo, M. N.; Frederix, P. W. J. M.; Periole, X.; Marrink, S. J. Exchange Pathways of Plastoquinone and Plastoquinol in the Photosystem II Complex. *Nat. Commun.* **2017**, 8 (1), 1–8.

- (39) Singharoy, A.; Maffeo, C.; Delgado-Magnero, K. H.; Swainsbury, D. J. K.; Sener, M.; Kleinekathöfer, U.; Vant, J. W.; Nguyen, J.; Hitchcock, A.; Isralewitz, B.; et al. Atoms to Phenotypes: Molecular Design Principles of Cellular Energy Metabolism. *Cell* **2019**, *179* (5), 1098–1111.
- (40) Sener, M.; Strumpfer, J.; Singharoy, A.; Hunter, C. N.; Schulten, K. Overall Energy Conversion Efficiency of a Photosynthetic Vesicle. *eLife* **2016**, *5*, No. e09541.
- (41) Arnarez, C.; Mazat, J.-P.; Elezgaray, J.; Marrink, S.-J.; Periole, X. Evidence for Cardiolipin Binding Sites on the Membrane-Exposed Surface of the Cytochrome Bc1. *J. Am. Chem. Soc.* **2013**, *135* (8), 3112–3120.
- (42) Arias-Cartin, R.; Grimaldi, S.; Pommier, J.; Lanciano, P.; Schaefer, C.; Arnoux, P.; Giordano, G.; Guigliarelli, B.; Magalon, A. Cardiolipin-Based Respiratory Complex Activation in Bacteria. *Proc. Natl. Acad. Sci. U. S. A.* **2011**, *108* (19), 7781–7786.
- (43) Corey, R. A.; Pyle, E.; Allen, W. J.; Watkins, D. W.; Casiraghi, M.; Miroux, B.; Arechaga, I.; Politis, A.; Collinson, I. Specific Cardiolipin–SecY Interactions Are Required for Proton-Motive Force Stimulation of Protein Secretion. *Proc. Natl. Acad. Sci. U. S. A.* **2018**, 115 (31), 7967–7972.
- (44) Robinson, C. V. Mass Spectrometry: From Plasma Proteins to Mitochondrial Membranes. *Proc. Natl. Acad. Sci. U. S. A.* **2019**, *116* (8), 2814–2820.
- (45) Tocilescu, M. A.; Zickermann, V.; Zwicker, K.; Brandt, U. Quinone Binding and Reduction by Respiratory Complex I. *Biochim. Biophys. Acta, Bioenerg.* **2010**, *1797* (12), 1883–1890.
- (46) Zwicker, K.; Galkin, A.; Dröse, S.; Grgic, L.; Kerscher, S.; Brandt, U. The Redox-Bohr Group Associated with Iron-Sulfur Cluster N2 of Complex I. J. Biol. Chem. 2006, 281 (32), 23013—23017.
- (47) Couch, V.; Popovic, D.; Stuchebrukhov, A. Redox-Coupled Protonation of Respiratory Complex I: The Hydrophilic Domain. *Biophys. J.* **2011**, *101* (2), 431–438.
- (48) Chang, C. H.; Kim, K. Density Functional Theory Calculation of Bonding and Charge Parameters for Molecular Dynamics Studies on [FeFe] Hydrogenases. *J. Chem. Theory Comput.* **2009**, *5* (4), 1137–1145.
- (49) Freddolino, P. L.; Gardner, K. H.; Schulten, K. Signaling Mechanisms of LOV Domains: New Insights from Molecular Dynamics Studies. *Photochem. Photobiol. Sci.* **2013**, *12* (7), 1158–1170.
- (50) de Vries, S.; Dörner, K.; Strampraad, M. J. F.; Friedrich, T. Electron Tunneling Rates in Respiratory Complex I Are Tuned for Efficient Energy Conversion. *Angew. Chem., Int. Ed.* **2015**, *54* (9), 2844–2848.
- (51) Zu, Y.; Di Bernardo, S.; Yagi, T.; Hirst, J. Redox Properties of the [2Fe-2S] Center in the 24 KDa (NQO2) Subunit of NADH:Ubiquinone Oxidoreductase (Complex I). *Biochemistry* **2002**, *41* (31), 10056–10069.
- (52) Hinchliffe, P.; Carroll, J.; Sazanov, L. A. Identification of a Novel Subunit of Respiratory Complex I from Thermus Thermophilus. *Biochemistry* **2006**, *45* (14), 4413–4420.
- (53) Singharoy, A.; Teo, I.; McGreevy, R.; Stone, J. E.; Zhao, J.; Schulten, K. Molecular Dynamics-Based Refinement and Validation for Sub-5 Å Cryo-Electron Microscopy Maps. *eLife* **2016**, *S*, No. e16105.
- (54) Aird, A.; Wrachtrup, J.; Schulten, K.; Tietz, C. Possible Pathway for Ubiquinone Shuttling in Rhodospirillum Rubrum Revealed by Molecular Dynamics Simulation. *Biophys. J.* **2007**, 92 (1), 23–33.
- (55) Singharoy, A.; Chipot, C.; Moradi, M.; Schulten, K. Chemomechanical Coupling in Hexameric Protein—Protein Interfaces Harnesses Energy within V-Type ATPases. J. Am. Chem. Soc. 2017, 139 (1), 293–310.
- (56) Free Energy Calculations: Theory and Applications in Chemistry and Biology; Chipot, C., Pohorille, A., Eds.; Springer Series in Chemical Physics; Springer-Verlag: Berlin/Heidelberg, 2007. DOI: 10.1007/978-3-540-38448-9.

(57) Hummer, G. Position-Dependent Diffusion Coefficients and Free Energies from Bayesian Analysis of Equilibrium and Replica Molecular Dynamics Simulations. *New J. Phys.* **2005**, 7 (1), 34.